Ordering and growth of Xe films on the 10-fold quasicrystalline approximant Al_{13}Co_{4}(100) surface

Heekeun Shin, M. Karimi, W. Setyawan, S. Curtarolo, and R. D. Diehl

The ordering and growth of Xe films on the 10-fold quasicrystalline approximant $Al_{13}Co_4(100)$ surface

Heekeun Shin[1], M. Karimi[2], W. Setyawan[3], S. Curtarolo[3] and R. D. Diehl[1]

[1]Department of Physics, Penn State University, University Park, PA 16802

[2]Department of Physics, Indiana University of PA, Indiana, PA 15705

[3]Department of Materials Science and Mechanical Engineering, Duke University, Durham, NC 27708

Abstract

Xe adsorption on the (100) surface of the complex alloy $Al_{13}Co_4$ has been carried out using low-energy electron diffraction (LEED) and grand canonical Monte Carlo (GCMC) simulations. This surface is an approximant to the 10-fold surface of decagonal Al-Ni-Co, on which Xe adsorption had been studied earlier. The adsorption behavior on the periodic surface is largely similar to that on the quasicrystal (layer-by-layer growth, hexagonal ordering near the onset of the 2nd-layer adsorption) but also has some differences, such as the complete lack of registry of the Xe layer with the substrate structure in the hexagonal phase, and a high sensitivity of the Xe epitaxial direction to trace impurities. An ordering transition between the low-density and high-density monolayer regimes was observed in the simulations, which involves a uniaxial compression of the monolayer film.

I. Introduction

The physical behavior of systems involving competing interactions is a subject of continuing interest. The growth of thin films of a single element on quasicrystal surfaces almost always involves competing interactions because the natural crystalline structure of the low-energy facets of crystals is generally periodic. Several recent reviews of film growth on quasicrystal surfaces [1-4] have enumerated the various growth modes that have been observed. While the first layer frequently adopts a quasicrystalline structure that matches the substrate, most ordered multilayer films have periodic structures and involve some kind of matching of the film structure to the substrate structure. This can occur on a local scale, such as when the interface involves an aperiodic vicinal plane of the periodic crystal [5], or in a more extended scale with a higher-order commensuration that appears as a moiré structure in images of the film [6].

A great deal of insight into the physical mechanisms responsible for different types of growth can be obtained from the study of rare gas interactions with surfaces since their interactions are relatively simple and are readily modeled [7,8]. An earlier study of rare gas adsorption on a 10-f decagonal Al-Co-Ni quasicrystal surface established that the existence of long-range order in a rare gas film depends entirely on the relative length scales of the gas (atom size) and the quasicrystal (average lattice parameter) [9-14]. This is also a characteristic of many of the metal films that have been studied [4].

In the last decade, large single crystals of "quasicrystalline approximants [15,16] have become available. These are materials that typically lie close to quasicrystal phases in the alloy phase diagram, and have local structures that are very similar to those found in quasicrystals. However, their long-range order is periodic rather than aperiodic, and this periodicity greatly facilitates their structure determination. Since samples have only recently become available in large enough sizes for most surface techniques [17-21], there are very few studies of growth on these surfaces [22]. In this study, we have performed adsorption studies of Xe on the pseudo-10-f surface of orthorhombic $Al_{13}Co_4(100)$ [23], which is an approximant of the 10-fold surface of the decagonal Al-Co-Ni quasicrystal, which was studied earlier [9-11,24,25].

$Al_{13}Co_4$ has 102 atoms per unit cell, and its orthorhombic lattice parameters are $a = 8.158$ Å, $b = 12.342$ Å and $c = 14.452$ Å as determined from x-ray diffraction [23]. Its structure along the [100] direction can be described as the stacking of two types of layers, flat (F) having 17 Al and 8 Co atoms, and puckered (P), having 22 Al and 4 Co atoms. There are two types of each plane, producing a stacking sequence $P_1F_1P_2F_2$ and a separation between planes of about 2 Å.

The structure of this $Al_{13}Co_4(100)$ crystal surface was studied earlier using LEED, STM and DFT [26, 27] and the crystal was found to terminate in a 50:50 mixture of the two P planes. The surface P planes are similar to the bulk P layers, but are missing the 4 Co atoms per unit cell in the top layer [26]. The diagram of the top layer of one of the P terminations is shown in Figure 1, along with two LEED patterns, one of which clearly shows the pseudo-10-f nature of this periodic crystal. The model drawing shows the bi-pentagonal arrangement of Al atoms at the surface. These bipentagons result from a cut through the pyramidal clusters that are the building blocks of this crystal structure. The relationship between the two P layers in the bulk is that the direction of their "pucker" is related by a mirror reflection with respect to the intervening F layer. The relationship between the two P terminations on the surface, aside from some small differences in puckering amplitudes, is a reflection in the vertical or horizontal directions of the model shown in Figure 1c.
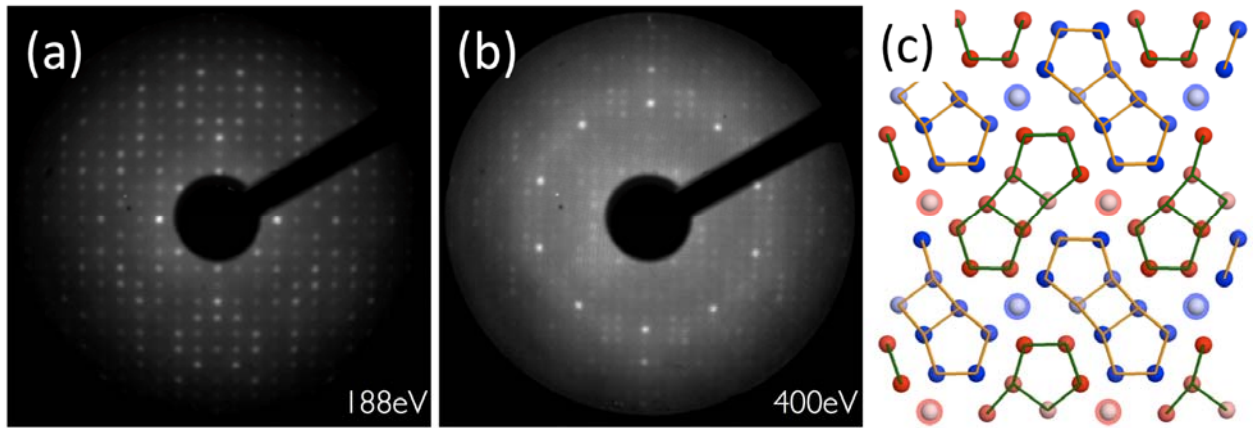

Figure 1. (color online) (a, b) LEED patterns at primary beam energies 188 eV and 400 eV, respectively, at a sample temperature of 80 K. (c) Diagram of the top layer atoms of $Al_{13}Co_4(100)$ unit cell. Blue (red) corresponds to atoms above (below) the center of mass of the layer, the color shading indicates the magnitude of the displacement from the center of mass of the layer. All atoms are Al, the large ones are the "glue" atoms between the bipentagons.

II. Experiment and Simulation Procedures

The Al$_{13}$Co$_4$ sample used in this study was grown from Al-rich solutions using the Czochralski method [15].   This phase is stable to 950°C. The crystal was oriented using Laue x-ray diffraction, cut perpendicular to the [100] direction, and then mechanically polished using diamond paste with decreasing grain size down to 0.25 µm and using Syton for the final polishing.   Preparation in ultra-high vacuum involved cycles of 0.5 keV Ar+ bombardment and long (several hours) anneals as high as 900°C.   The annealing temperature of the crystal was measured using an infrared pyrometer with the emissivity set at 0.35.

The LEED intensities were measured using a rear-view LEED system, with the electron beam at normal incidence to the surface. The data were acquired using a monochromatic charge-coupled-device (CCD) camera interfaced through a personal computer via a Data Translation frame grabber board. The LEED adsorption isobars were obtained by holding the Xe pressure in the chamber at a fixed value while changing the temperature and acquiring LEED frames. During these measurements, the temperature was measured using a chromel-alumel thermocouple in contact with the sample.   The integrated spot intensities were then extracted from the saved LEED patterns.

The simulations were carried out using the grand canonical Monte Carlo (GCMC) method. The simulation procedure has been described in detail previously [9, 11, 13]. For a given volume (V) and temperature (T), the configurational phase space is explored using the Metropolis algorithm to find the equilibrium number of adsorbed atoms (N) as a function of the chemical potential (μ) of the Xe. μ is related to the pressure of the coexisting Xe gas by assuming an ideal gas. Then we obtain the adsorbed density isotherms as a function of the pressure, $P(T, \mu)$. For each data point in an isotherm, 8 million MC steps were performed to reach nominal equilibrium and another 8 million steps were performed in the subsequent data-gathering stage. Each MC step is an attempted creation, deletion, or displacement of an atom with an execution probability equal to 0.4, 0.4, and 0.2, respectively[9, 11, 13].

The interaction potentials used in the simulations are based on the 12-6 Lennard-Jones (L-J) pair interaction. The adsorption potential is taken to be a sum of L-J pair potentials between Xe-Al and Xe-Co. The coordinates of the Al and Co atoms in the substrate, as well as the L-J

interactions parameters, are adopted from previous work [9-11]. The Xe-Xe interaction size and energy parameters are $\sigma_{gg} = \sigma_{Xe} = 0.41$ nm and $\varepsilon_{gg} = \varepsilon_{Xe} = 19$ meV. The adsorption potential parameters are derived from traditional combining rules, resulting in the values $\sigma_{Xe-Al} = 0.33$ nm, $\varepsilon_{Xe-Al} = 24$ meV, $\sigma_{Xe-Co} = 0.31$ nm, and $\varepsilon_{Xe-Co} = 23$ meV.

The simulations are performed in an orthorhombic cell. The height of the cell, which is along the z direction, is chosen to be 10 nm (high enough to contain at least 25 layers of Xe). At the top of the cell, a hard-wall reflective potential is simulated to confine the vapor. The base of the cell has a dimension of 24.684 Å x 28.904 Å, i.e. 4 surface unit cells in area. Periodic boundary conditions are employed along the x and y directions. We used a fairly large cutoff (5 σ_{gg}) to minimize long-range interaction corrections.

III. LEED Results

During the Xe adsorption experiments, it was found that the Xe film is particularly sensitive to impurity adsorption. We note that this was not the case on the quasicrystal surface [24]. Although there was no observable degradation of the LEED pattern over the course of an experiment lasting 1 hour, the nature of the adsorption of Xe and the structures formed changed. The source of the impurity is not known, but its adsorption only occurred in the presence of the electron beam. The impurity was not detectable in the Auger spectrum even after many hours in the electron beam, suggesting that its level may saturate at a low level. However, it was not possible to obtain adsorption data for the Xe film that are entirely free of the impurity effects. Since the impurity induces a different Xe structure, however, it is relatively easy to separate the clean-surface adsorption behavior from the impurity-induced adsorption behavior.

Figure 2a shows a LEED pattern from the clean surface and Figure 2c shows a LEED pattern of the surface with ordered Xe present. In both panels, the locations of the (2,3) and equivalent diffraction spots of the substrate are indicated. The fact that some of the Xe overlayer spots coincide with the the (2,3) spots indicates a commensurability of the Xe with the substrate. In Figure 2b, a similar diffraction pattern to that in 2c is shown, but with the intensity inverted for clarity. In this pattern, two sets of 12 diffraction spots have been identified and labeled, each corresponding to two domains of a hexagonal Xe lattice that is rotated relative to the substrate. The red circles identify one set of spots that include those at the (2,3) substrate positions, the

blue squares identify the other set, which has no commensurability with the substrate. Figure 2d indicates the range of an azimuthal intensity profile through the spots, shown in Figure 2e, which indicates that the "commensurate" spots subtend angles of $\pm 22.02°$ relative to the y-axis (which is the short axis in reciprocal space), and the "incommensurate" spots subtend angles of $\pm 14.32°$. For both types of Xe domains, the measured Xe-Xe distance is 4.40 ± 0.05 Å
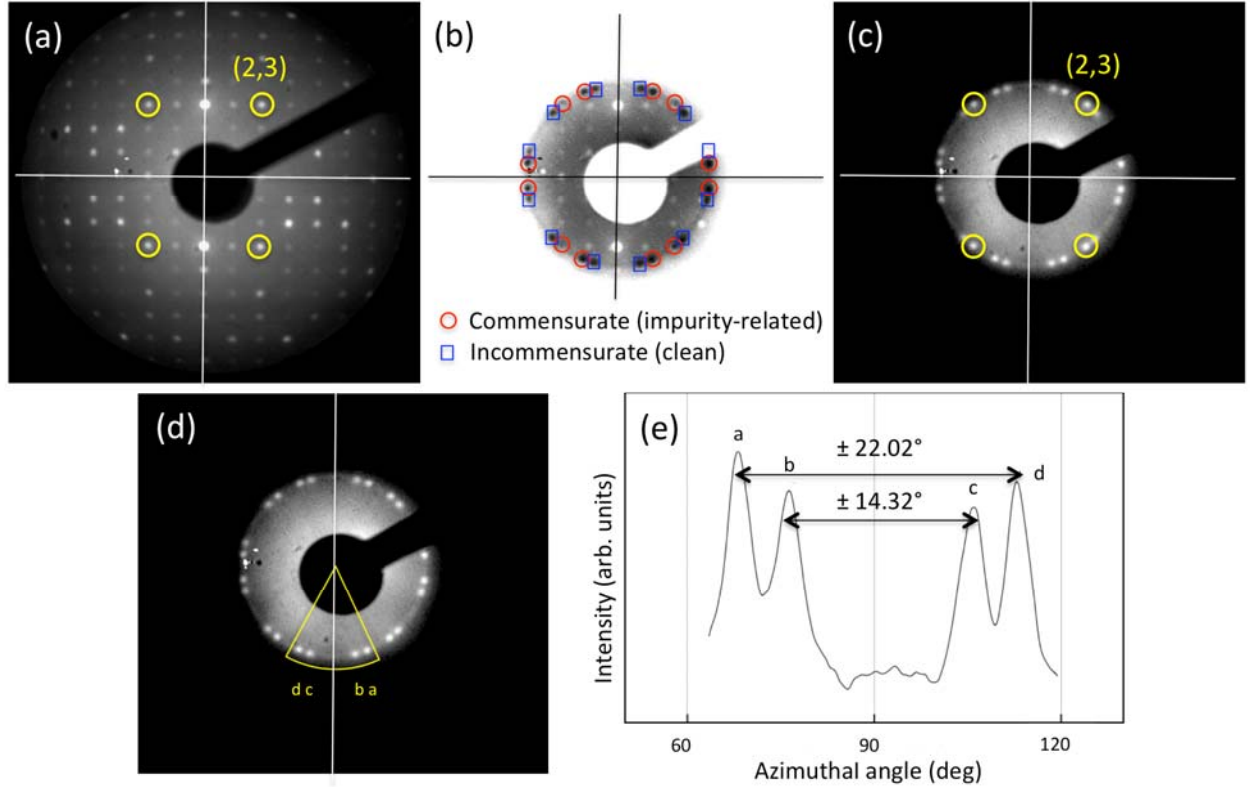

Figure 2. (color online) (a) LEED pattern from the clean $Al_{13}Co_4$ surface at 65 eV. The (2,3) and equivalent diffraction spots are indicated by circles. (b-d) LEED patterns at the same energy after the ordering of Xe on the surface. (b) (intensity inverted for clarity) indicates the two differently rotated domains of hexagonal Xe (red circles and blue squares). (c) shows that one of these domains (red circles in (b) - commensurate) has diffraction spots that are coincident with the substrate (2,3) spots. (d) indicates the range of an intensity profile shown in (e), which shows that the lattice angles subtended by the two different types of hexagonal Xe are $\pm 14.32°$ and $\pm 22.02°$.

In Figure 2, the diffraction patterns from the two types of domains have nearly equal intensities. However, during the course of the data acquisition, the spots corresponding to the "incommensurate" structure were more intense in the early measurements, while those from the "commensurate" structure were more intense in later experiments. Figure 3 shows this progression over the course of isobar measurements that were conducted over a period of about 1 hour.
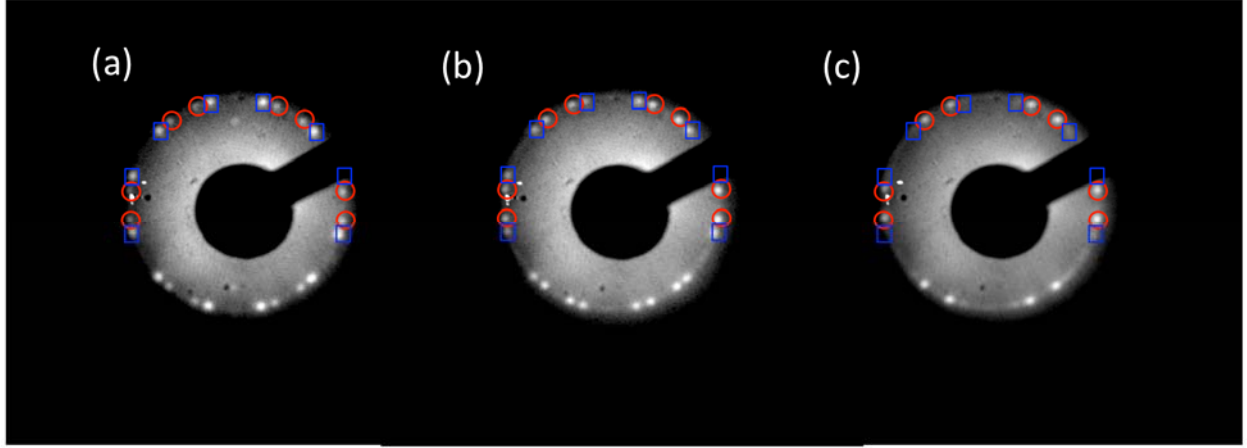
Figure 3. (color online) LEED patterns from an ordered Xe film, taken consecutively during the course of adsorption experiments that lasted about 1 hour. In the early experiments, the Xe is mostly in the "incommensurate" phase (red circles). This phase was gradually replaced by the "commensurate" phase (blue squares).

Figure 4a shows the LEED spot intensities for selected beams during an isobaric adsorption experiment carried out at a Xe pressure of 7×10^{-6} mbar. Curves 1 and 2 correspond to substrate spots, and have relatively high intensity at T = 70 K before the adsorption begins. As the temperature is lowered, there is a stepwise decrease in their intensities at about 66 K. This corresponds to the adsorption of the first layer of Xe, and there is no evidence of Xe ordering at this stage of adsorption. A second step is evident at about 60 K, and this corresponds to the second layer of Xe. After the second layer, additional steps are evident in curve 1 for the 3rd and 4th layers of Xe at about 58 K and 57 K, respectively. At the same time, increasing-intensity steps are evident in curve 2, since this curve represents the intensity at a (3,2) position, where there is both substrate and "commensurate" Xe layer diffraction. A fifth step is evident at about 56 K for this curve. At the same time, curves 3 and 4 show increases in intensity corresponding to the ordering of Xe in both the "commensurate" and "incommensurate" structures, respectively. It is worth noting that this isobar was done fairly late in the experiment, and so the "commensurate" spots are more intense and the "incommensurate" spots are barely detectable.
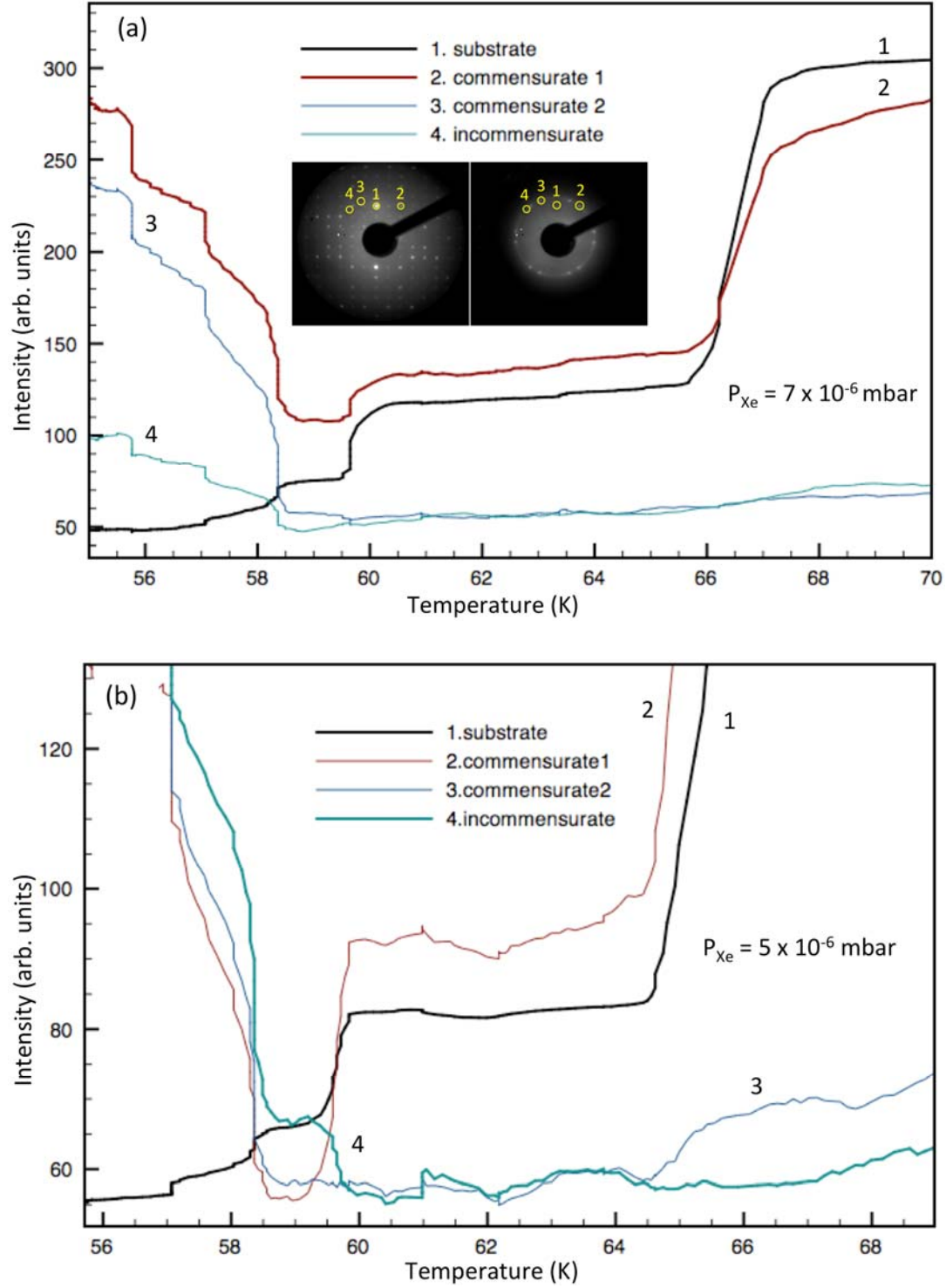
Figure 4. (color online) (a) LEED intensity isobars for Xe adsorption at a constant pressure of 7 x 10^{-6} mbar. (b) LEED intensity isobars for Xe adsorption at a Xe pressure of 5 x 10^{-6} mbar, enlarged to show the details at the second-layer adsorption step (near 60 K).

Figure 4b shows a similar isobaric measurement at 5 x 10^{-6} mbar, which was performed earlier in the series and therefore has more of the "incommensurate" structure. This graph is magnified to show the intensities at the onset of the adsorption of the second layer of Xe. As before, curves 1 and 2 show decreasing steps at about 65 K and 60 K due to the attenuation of the scattering from the substrate, and curve 4, corresponding to the "incommensurate" phase that grows on the clean substrate, increases during the adsorption of the second layer, and again at about 58 K when the 3rd layer adsorbs. Curve 3, on the other hand, which is due solely to the "commensurate" Xe that forms on the contaminated surface, only shows a significant increase when the 3rd layer adsorbs. This indicates that the "incommensurate" Xe orders at an earlier stage, suggesting that the impurities may interfere with the ordering of the "commensurate" phase. Curve 2, which is also from the "commensurate" phase, also increases at the 3rd-layer step. The lack of Xe ordering upon adsorption of the monolayer of Xe, which is quite unusual on simpler surfaces [28], was also observed on the quasicrystal surface studied before, and in that case was found to be a result of the Xe adopting the symmetry of the substrate at low coverages [9, 24].

To summarize the LEED results, the Xe overlayer behavior on $Al_{13}Co_4$(100) is extremely sensitive to impurity adsorption, much more sensitive than has been observed on other metal surfaces or on the Al-Co-Ni quasicrystal surface. Ordering on the clean surface occurs during adsorption of the second layer of Xe, and its structure is hexagonal, incommensurate, and rotated ±14.32° from the long (c) axis of the substrate unit cell. On the slightly contaminated surface, the growth is also layer-by-layer, but ordering occurs during the formation of the third layer. The structure is hexagonal and rotated at ±22.02° relative to the long substrate axis, making its lattice partially coincident with the substrate lattice, sharing diffraction spots at the substrate (2,3) position.

IV. Simulation Results

The calculated adsorption potential for Xe on the P2 termination of $Al_{13}Co_4$ shown in Figure 1 is shown in Figure 5a. The average potential energy is 167 meV and its root-mean-square corrugation amplitude, estimated from the standard deviation, is 22 meV (13%). The adsorption energy is somewhat weaker than that for Xe adsorption on the Al-Co-Ni quasicrystal surface [9], mainly due to the absence of the four Co atoms in the surface layer, which reduces the density of

the surface. The corrugation is also smaller compared to the quasicrystal case (rms = 50 meV). In Figure 5a, the atoms of the top layer, which is entirely composed of Al, are superimposed on the adsorption potential map. As mentioned earlier, the top layer is puckered: the atoms in red are located lower than those in blue. Consequently, the strongest adsorption sites at sub-monolayer coverage are found at the centers of the red bipentagons. At higher coverages, these sites are not necessarily occupied, as described later in the discussion of the density profile of the adsorbed layer.
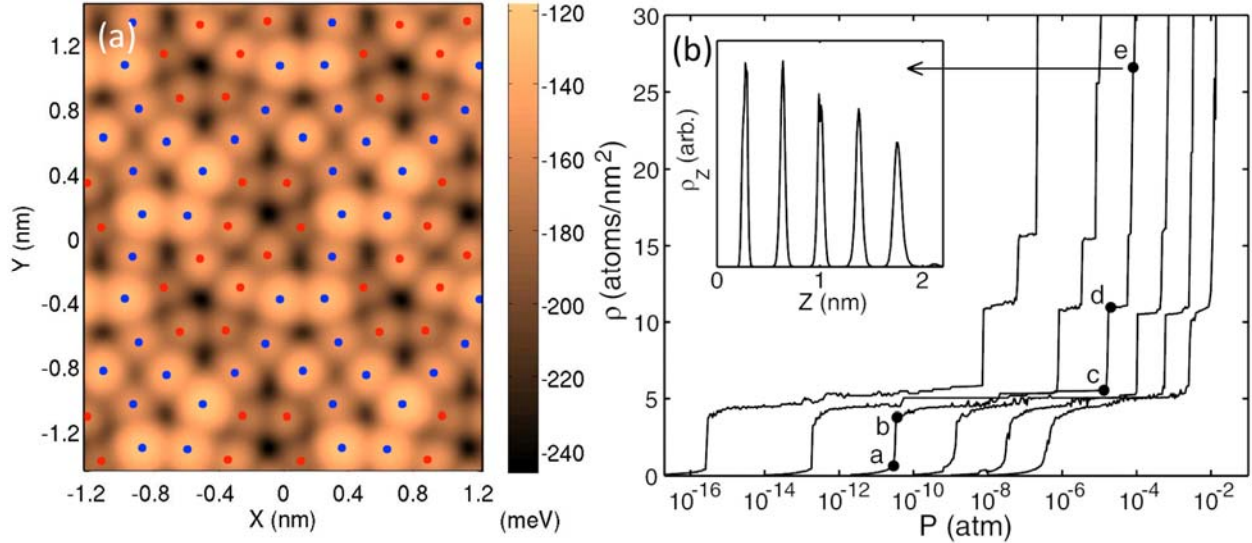

Figure 5. (color online) (a) Calculated adsorption potential for Xe on $Al_{13}Co_4$. (b) Calculated adsorption isotherms for Xe on $A_{13}Co_4$. The simulated temperatures are 60 K to 110 K with 10 K increment. The inset depicts the density profile along the z-axis at 80 K and shows the five adsorbed layers of Xe at a pressure corresponding to point e.

The adsorption isotherms are plotted in Figure 5b. The growth of the Xe film was simulated at temperatures 60, 70, 80, 90, 100, and 110 K. The isotherm at 60 K corresponds to the left-most plot in Figure 5b. In each plot, a vertical riser indicates the formation of an additional layer. At low temperatures, plateaus displaying a successive formation of the first three layers are evident before the bulk condensation occurs. This layer-by-layer growth is a consequence of the weaker attraction of a Xe atom to a close packed surface of Xe film as compared to that between a Xe atom and the $Al_{13}Co_4$ surface. In our previous study on the 10-f Al-Ni-Co surface, we simulated fictitious gases with increasing interaction strength while maintaining the same average adsorption potential[13]. We found that the relative strength of the competing interactions determines the growth mode. Clustering occurs when the adsorbate-adsorbate attraction is stronger than the adsorption potential. In this work, the simulated temperatures are below the

triple-point temperature of Xe, which is 161.4 K. For this system, solid Xe films with well-resolved layering is observed in all isotherms. This is illustrated in the inset of Figure 5b with a plot of the density profile along the z-direction at a pressure corresponding to point (e) in the 80-K isotherm.

The probabilistic locations of the adsorbed atoms during the formation of the monolayer are depicted in the top panel of Figure 6. These density profiles are from the simulation at 80 K. Their Fourier transforms (FT) are plotted in the bottom panels. The left, middle, and right plots are taken at pressures that correspond to points a, b, and c in Figure 5b. As mentioned earlier, in the sub-monolayer regime, Xe atoms occupy the center of the lower (red) bipentagons. Interestingly, at the onset of the monolayer formation, the atoms migrate to the neighboring but less attractive sites as demonstrated by the vacancies of the red bipentagons in the middle plot. At this coverage, to minimize the total energy of the layer, the atoms jump to the center of the higher (blue) bipentagons. They also occupy the centers of other quasi-pentagonal sites, which are composed of two red and three blue substrate atoms. The overall ordering at this point is revealed to be uniaxially-compressed hexagonal in the FT plot. Six spots are marked with circles in the FT to highlight the quasi-hexagonal ordering of the atoms. At the completion of the first layer (right panel), a nearly-symmetric hexagonal structure is observed. The FT confirms the long-range ordering with nearly 6-fold symmetry. More details of this ordering are provided in Section V.
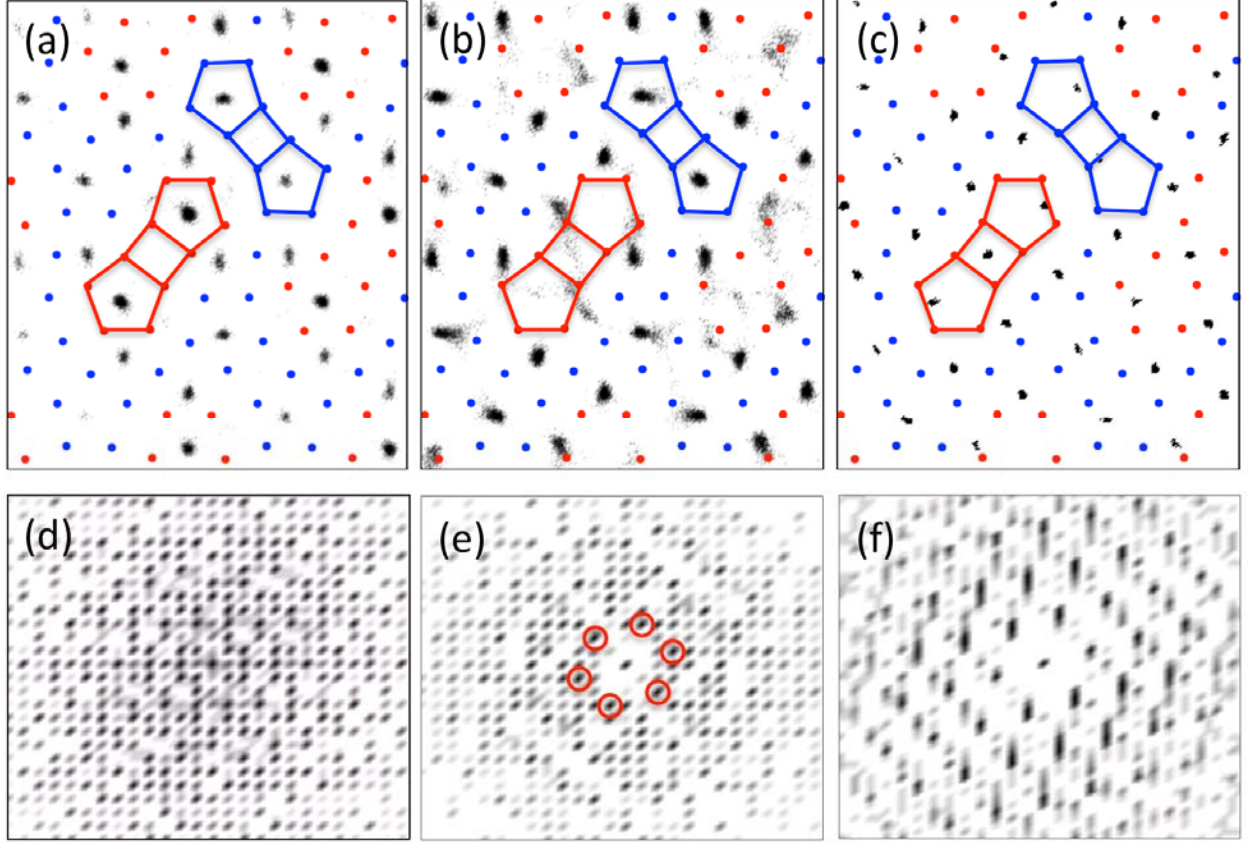
Figure 6. (color online) Density plots showing the probabilistic location of the adsorbed Xe atoms at 80 K (top panel) and their FT's (bottom panel). The left, middle, and right plots correspond to the submonolayer, the onset of monolayer, and the full monolayer coverages, respectively. The apparent high resolution (fine structure) of the FT's, especially in (d) and (e), is a consequence of the periodic boundary conditions and reflects the size of the simulation cell.

The structure of the monolayer at the onset of its formation (center panels in Figure 6) does not exhibit any long-range order. The resolvable ordering is a short-range hexagonal structure, which is due to the local arrangements of the atoms. A structural transition from short-range to long-range hexagonal ordering occurs during the completion of the first layer. To investigate the nature of the transition, the evolution of the average nearest neighbor distance (d_{NN}) as a function of coverage is studied. The d_{NN} is calculated by assuming a perfect hexagonal structure for a given number of adsorbed atoms. In this way, d_{NN} is directly related to the adatom density. We define a normalized chemical potential (μ^*) as follows [9]:

$$\mu^* = \frac{\mu - \mu_1}{\mu_2 - \mu_1}$$

where μ_1 and μ_2 are the chemical potential at the onset and completion of the monolayer, respectively. In the middle panel of Figure 7, d_{NN} is plotted as a function of μ^*. A rather abrupt

drop approximately at μ* = 0.5 (as indicated by the arrow) is caused by a simultaneous addition of 3 to 4 atoms per unit cell in the monolayer. It is at this point that the long-range order is established. The change is accompanied by a decrease of the total enthalpy (approximately 0.6 eV) as shown in the bottom panel. Therefore, the transition may be first-order with the associated latent heat.
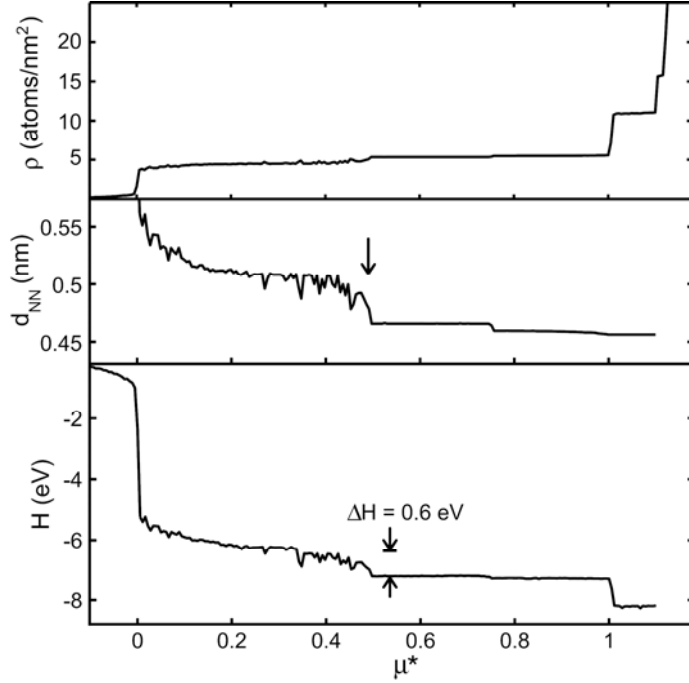

Figure 7. Xe adsorption at 80 K: (top panel) adsorption isotherm, (middle panel) nearest neighbor distance by assuming a hexagonal structure, and (bottom panel) total enthalpy of the system as a function of the normalized chemical potential as defined in the text. The arrow in the middle panel indicates the location of a possible first-order transition, and the associated enthalpy is indicated in the bottom panel.

Thermodynamically, heat of adsorption on a corrugated substrate depends on the adlayer coverage. In a system that exhibits layer-by-layer growth, the heat of adsorption decreases as the number of adsorbed layers increases. For a given coverage (n), the isosteric heat of adsorption per atom (q_{st}) can be calculated from the adsorption phase diagram as follows:

$$q_{st} = -k_B \frac{\partial(\ln P)}{\partial(1/T)}\bigg|_n$$

In Figure 8, the adsorption phase diagram is constructed from three different coverages. The plotted quantities are the pressure and temperature *loci* of the first three vertical risers in the isotherms. Hence the data correspond to approximately 0.5, 1.5, and 2.5 monolayer coverages. The calculated isosteric heats of adsorption are 241, 145, and 135 meV, respectively. The

corresponding values obtained in the quasicrystal study were 270, 129 and 125 meV, respectively [11]. In both cases, the heats of condensation for the second and third layer are slightly lower than the bulk value of 165 meV [24]. The discrepancy originates from the small inaccuracy in the Xe-Xe interaction parameters.
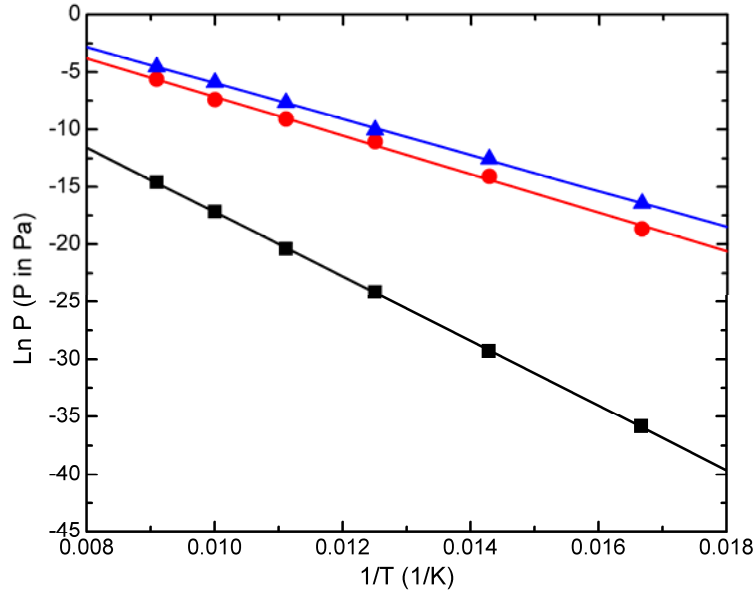

Figure 8. (color online) Pressure and temperature *loci* of the onset of the first layer (square), second layer (circle), and third layer (triangle) formation of Xe on $Al_{13}Co_4(100)$ surface. The corresponding isosteric heats of adsorption are 241, 145, and 135 meV, respectively.

V. Discussion

A comparison of the experimental and simulated results for the adsorption of Xe indicates a quantitative similarity in the pressure-temperature conditions for adsorption, and both indicate layer-by-layer adsorption of the Xe. The experiments did not detect the short-range quasihexagonal ordering observed in the simulations in the low-density monolayer, but both indicated long-range hexagonal order at or near the onset of the second layer. We examine this hexagonal ordering in Figure 9a. The red lines indicate the symmetry directions in the FT. The deviation from true 6-fold symmetry can be ascertained from the angles given, and the positions of the FT features indicates an anisotropy of about 10% when comparing the 6 directions.
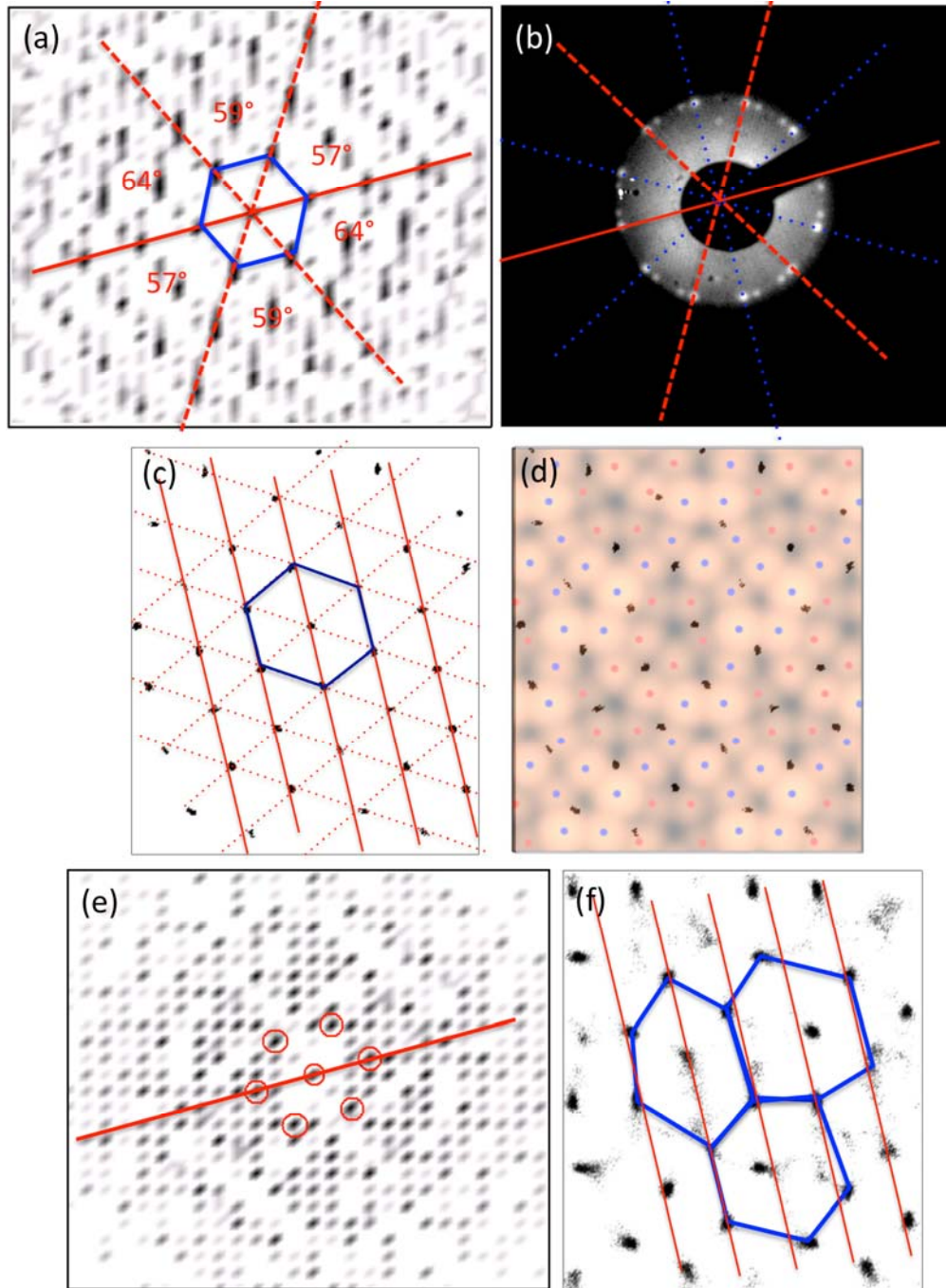
Figure 9. (color online) (a) FT from the high-density structure showing the primary symmetry directions. The solid red line establishes a primary symmetry direction that persists in all of the observations. (b) LEED pattern from the ordered structure, showing that the primary symmetry direction from (a) coincides with diffraction spots from one domain of the ordered (clean) structure. (c) Density plot for the high-density structure, showing the rows of Xe (solid red lines) that correspond to the primary symmetry direction, and the other close-packed directions (dashed lines). (d) Superimposition of the density plot (black represents Xe) onto the potential energy map, showing that Xe atoms are primarily located between surface Al atoms (red and blue dots). (e) FT from the low-density structure, indicating that the primary symmetry direction is maintained. (f) Density plot for the low-density structure with the solid red lines from (c), showing the ordering transition observed in the simulations involves a uniaxial compression along these lines.

15

The solid red line from Figure 9a is reproduced exactly on the LEED pattern shown in Figure 9b, and it can be seen to intersect one set of the diffraction spots. This indicates there is an exact alignment of one of the directions indicated in the FT from the simulations and one set of LEED spots shown in Figure 9a. Unlike the FT from the simulation, the LEED pattern shows true hexagonal symmetry, with angles of 60° between each of the red (solid or dashed) lines. The set of LEED spots corresponding to these lines is one orientation of the "clean" structure. The other set of "clean" diffraction spots is indicated by dotted blue lines, and originates from the other surface termination (not included in the simulation), related to the red ones by a reflection in the vertical or horizontal axis. The weaker diffraction spots that do not intersect any of the lines arise from the "impurity" structure.

Figure 9c shows the density plot corresponding to the same structure. The solid red lines indicate the rows of Xe atoms that produce the lowest-order peaks in the FT along the direction indicated by the solid red line in Figure 9a. The dashed lines indicate the rows of Xe atoms in the other directions. The blue lines indicate the distorted hexagonal structure formed by the Xe, and the angles within this hexagon correspond directly to those in the FT in Figure 9a. Figure 9d shows the density plot superimposed on the calculated potential energy. It is evident that while the Xe atoms may not occupy the lowest-energy position (centers of red pentagons), they all occupy sites between substrate atoms. The distortion from hexagonal apparently occurs in order to allow the Xe atoms to avoid high-energy sites, which would occur if the Xe lattice were perfectly hexagonal. The fact that the experiment indicates a perfectly hexagonal overlayer (to within the precision of the measurement) indicates that the actual corrugation experienced by the Xe is somewhat smaller than for the calculated potential.

It is interesting to compare this structure to the low-density structure observed in the simulation, even though it does not have good long-range order. Its FT is shown in Figure 9e, and the red line is at the same angle as that in Figure 9a, indicating that the Xe structure has one axis in common in both the low-density and high-density structures. The density plot shown in Figure 9f shows the same red lines as shown in Figure 9c, which on average line up with the rows of Xe atoms. Clearly, the average spacing of Xe atoms along these rows is significantly larger than that observed in the high-density structure, while the spacing between the lines is the same.

Therefore, the phase transition that occurs between the two structures involves a uniaxial compression along the rows of Xe atoms shown in Figure 9f, during which the overlayer establishes long-range order, which is nearly hexagonal.

The behavior of Xe adsorption on $Al_{13}Co_4$ shows both similarities and differences with the case of Xe adsorbed on the similar quasicrystalline Al-Co-Ni surface. In both cases, the Xe adsorbs in a layer-by-layer mode that is similar to the adsorption of Xe on simple metal surfaces. Long-range order is observed after monolayer adsorption and before second-layer adsorption in the simulation, whereas it occurs only with the onset of second-layer adsorption in the experiment. However, the structures that form are different. On the quasicrystal, Xe orders into a hexagonal structure that is coincident with an average quasicrystal spacing, producing diffraction spots that coincide with some of the substrate spots. On $Al_{13}Co_4$, the Xe also orders into a hexagonal structure (in the experiment), but there is no coincidence with the substrate diffraction spots. This appears to be because the average structure of $Al_{13}Co_4$ does not fit the inter-row spacing of Xe as well as the quasicrystal. On the quasicrystal surface, there were clear lines of lower potential energy that occurred on average 3.8Å apart, which is the natural inter-row spacing of Xe [9-11]. It is not possible to identify such low potential energy lines on this surface (see Figure 5), certainly none having an average spacing of 3.8 Å. Therefore, the Xe orders by finding local minima that are largely consistent with hexagonal order, resulting in a structure that has a different lattice orientation from the substrate. Such non-epitaxial lattice rotations are common for incommensurate physisorbed films and are understood to arise from a competition of the intra-overlayer and overlayer-substrate forces [29, 30], but a detailed analysis of that effect is beyond the scope of this paper. The fact that the monolayer structure in the simulation is slightly distorted relative to hexagonal, whereas it is consistent with hexagonal in the experiment, probably arises from the calculated corrugation being somewhat larger than the actual corrugation, as the latter includes electronic screening not considered in the calculations.

Although the presence of a phase transition from a low-density monolayer to a high-density monolayer is present on both $Al_{13}Co_4$ and the quasicrystal, there are qualitative differences. On the quasicrystal, the low-density film has 5-fold symmetry and a high degree of site order that is imposed by the substrate, whereas on $Al_{13}Co_4$, the low-density film has short-range

quasihexagonal order. Therefore, the phase transition on the quasicrystal is a symmetry-changing order-order transition, whereas on $Al_{13}Co_4$, it is a uniaxial compression from short-range "stretched hexagonal" order into long-range nearly-hexagonal ordering, more akin to a disorder-order transition. Nevertheless, in terms the conditions under which they happen, their abruptness, and their associated density and energy changes, the two transitions appear to be very similar. Neither transition is observed directly in the experiment, however, due to the difficulty of detecting the structures of either disordered overlayers, or overlayers having the same symmetry as the substrate.

We recall that the simulations presented here were carried out on just one of the two terminating "puckered" layers of the substrate. Although these two terminations have identical compositions, their surface relaxations are slightly different due to differences in the exact relationship of their atoms with the underlying flat layer. The simulations presented here were carried out on the P2 termination [26], which has a slightly larger spacing between the two top substrate layers than the P1 termination. We found in simulations on the P1 termination that the positions of the isotherm steps shifted slightly downward in pressure, consistent with stronger binding on this slightly denser surface. There was also a slight shift downward in the phase transition pressure. All other behavior was the same, aside from the mirror symmetric structures formed, which produce the second domain that is observed in the experimental diffraction patterns.

The effect of the impurity on the Xe adsorption is rather curious. First, the amount of impurity, which is most likely a cracking product of a common residual gas such as CO or CO_2, is exceedingly small. Such effects, also with exceedingly low levels of impurity adsorption, have been seen before in physisorbed films [31, 32]. In those cases, the physisorbed film was found to align with step edges, which were either blocked or activated by impurities adsorbed at them, and trace impurity adsorption has even been used to manipulate the orientational epitaxy of physisorbed films [33]. In this case, the fact that the Xe lattice shares a reciprocal lattice vector with the substrate indicates an alignment with the substrate, but that alignment is not along a unit cell vector. STM images suggest that the primary step directions are along the unit cell vectors, or along lines that connect the bipentagons, but these are not the directions of the Xe rows

according to the LEED pattern. It is possible that the impurity adsorbs in a way that changes the potential energy corrugation enough to cause the equilibrium structure to change. The Xe lattice parameter remains unchanged, in any case. In contrast to the present case, the Xe structure on the Al-Ni-Co quasicrystal was not very sensitive to impurity adsorption, although in that case, the equilibrium structure was already coincident with a substrate symmetry (and step) direction.

Finally, one of the main findings in the earlier simulation study, which compared the ordering of different rare gases on the quasicrystal [14], was that the relative length scales of the ordered gas film and the substrate was paramount to establishing long-range order in the film. For the substrate studied here, it is difficult to identify a length scale on the potential energy surface that is appropriate for Xe, and therefore one might expect that long-range order would not occur, and yet it does, under essentially identical conditions as on the quasicrystal. The most likely explanation is that the corrugation of the substrate potential, which is about half that for the quasicrystal, is not sufficiently strong to interfere with ordering. The slight distortion from hexagonal ordering in the simulation results suggest that even this calculated corrugation is larger than the true corrugation, which is perhaps not unexpected on a metallic surface.

To summarize, we have performed LEED and GCMC studies of Xe adsorption on the complex metallic alloy surface $Al_{13}Co_4(100)$, and compared the results to an earlier study on the 10-fold surface of the Al-Ni-Co quasicrystal, which has a related structure. The adsorption behavior is largely similar on the two surfaces, exhibiting layer-by-layer adsorption, hexagonal ordering that occurs near the onset of the second layer, and in the simulation, an ordering phase transition that occurs in the monolayer regime. The Xe film on the periodic surface differs from that on the quasicrystal by being oriented along a non-principal direction of the substrate. The simulation faithfully reproduces the experimental observation of this orientation, which appears to be a result of a competition of the hexagonal film structure with the substrate corrugation.

References

1.	H. R. Sharma, M. Shimoda and A. P. Tsai, Advances in Physics **56**, 403 (2007).

2.	V. Fournée, J. Ledieu and P. A. Thiel, J. Phys.: Condens. Matt. **20**, 310301 (2008).

3.	R. McGrath, J. A. Smerdon, H. R. Sharma, W. Theis and J. Ledieu, J. Phys: Condensed Matt. **22** (2010).

4.	J. A. Smerdon, J. Phys: Condensed Matt. **22**, 433002 (2010).

5.	K. Pussi, M. Gierer and R. D. Diehl, J. Phys: Condensed Matt. **21**, 474213 (2009).

6.	T. Deniozou, J. Ledieu, V. Fournée, D. M. Wu, T. A. Lograsso, H. I. Li and R. D. Diehl, Phys. Rev. B **79**, 245405 (2009).

7.	L. W. Bruch, R. D. Diehl and J. A. Venables, Reviews of Modern Physics **79**, 1381 (2007).

8.	L. W. Bruch, M. W. Cole and E. Zaremba, *Physical Adsorption: Forces and Phenomena*. (Dover Press, 2007).

9.	S. Curtarolo, W. Setyawan, N. Ferralis, R. D. Diehl and M. W. Cole, Physical Review Letters **95**, 136104 (2005).

10.	R. D. Diehl, N. Ferralis, K. Pussi, M. W. Cole, W. Setyawan and S. Curtarolo, Philos. Mag. **86**, 863 (2006).

11.	W. Setyawan, N. Ferralis, R. D. Diehl, M. W. Cole and S. Curtarolo, Phys. Rev. B **74**, 125425 (2006).

12.	R. D. Diehl, W. Setyawan, N. Ferralis, R. A. Trasca, M. W. Cole and S. Curtarolo, Philosophical Magazine **87**, 2973 (2007).

13.	W. Setyawan, R. D. Diehl, N. Ferralis, M. W. Cole and S. Curtarolo, Journal of Physics-Condensed Matter **19**, 016007 (2007).

14.	R. D. Diehl, W. Setyawan and S. Curtarolo, Journal of Physics-Condensed Matter **20**, 314007 (2008).

15.	P. Gille and B. Bauer, Cryst. Res. Technol. **43**, 1161 (2008).

16.	W. Steurer, Mat. Res. Soc. Symp. **643**, K3.2.1 (2001).

17.	T. Deniozou, R. Addou, A. K. Shukla, M. Heggen, M. Feuerbacher, M. Krajcí, J. Hafner, R. Widmer, O. Gröning, V. Fournée, J. M. Dubois and J. Ledieu, Physical Review B **81**, 125418 (2010).

18.   R. Mäder, R. Widmer, B. Bauer, P. Gille, P. Gröning, W. Steurer and O. Gröning, Phys. Rev. B **81**, 064201 (2010).

19.   R. Mäder, R. Widmer, P. Gröning, P. Ruffieux, W. Steurer and O. Gröning, New J. Phys. **12**, 073043 (2010).

20.   R. Widmer, R. Mäder, M. Heggen, M. Feuerbacher and O. Grening, **88**, 2095 (2008).

21.   J. A. Smerdon, J. Parle, R. McGrath, B. Bauer and P. Gille, Z. Kristallogr. **224**, 13 (2009).

22.   V. Fournée, A. R. Ross, T. A. Lograsso, J. W. Anderegg, C. Dong, M. Kramer, I. R. Fisher, P. C. Canfield and P. A. Thiel, Phys. Rev. B **66**, 165423 (2002).

23.   J. Grin, U. Burkhardt, M. Ellner and K. Peters, Journal of Alloys and Compounds **206**, 243 (1994).

24.   N. Ferralis, R. D. Diehl, K. Pussi, M. Lindroos, I. R. Fisher and C. J. Jenks, Phys. Rev. B **69**, 075410 (2004).

25.   R. A. Trasca, N. Ferralis, R. D. Diehl and M. W. Cole, J. Phys: Condens. Mat. **16**, S2911 (2004).

26.   H. Shin, K. Pussi, E. Gaudry, J. Ledieu, V. Fournée, S. Alarcón Villaseca, Y. Grin, P. Gille, W. Moritz and R. D. Diehl, Phys. Rev. B **84**, 085411(2011).

27.   R. Addou, E. Gaudry, T. Deniozou, M. Heggen, M. Feuerbacher, P. Gille, Y. Grin, R. Widmer, O. Gröning, V. Fournée, J. M. Dubois and J. Ledieu, Phys. Rev. B **80**, 014203 (2009).

28.   R. D. Diehl, T. Seyller, M. Caragiu, G. S. Leatherman, N. Ferralis, K. Pussi, P. Kaukasoina and M. Lindroos, J. Phys.: Condens. Matt. **16**, S2839 (2004).

29.   J. P. McTague and A. D. Novaco, Phys. Rev. B **19**, 5299 (1979).

30.   A. D. Novaco and J. P. McTague, Phys. Rev. Lett. **38**, 1286 (1977).

31.   K. Kern, P. Zeppenfeld, R. David, R. L. Palmer and G. Comsa, Phys. Rev. Lett. **57**, 3187 (1986).

32.   G. S. Leatherman and R. D. Diehl, Langmuir **13**, 7063 (1997).

33.   G. S. Leatherman, R. D. Diehl, M. Karimi and G. Vidali, Phys. Rev. B **56**, 6970 (1997).